chemosensors

Article

Theoretical Design of Composite Stratified Nanohole Arrays for High-Figure-of-Merit Plasmonic Hydrogen Sensors

Jiyu Feng, Yuting Liu, Xinyi Chen, Mingyu Cheng and Bin Ai *

Chongqing Key Laboratory of Bio-Perception & Intelligent Information Processing, School of Microelectronics and Communication Engineering, Chongqing University, Chongqing 401331, China
* Correspondence: binai@cqu.edu.cn

Abstract

Fast, spark-free detection of hydrogen leaks is indispensable for large-scale hydrogen deployment, yet electronic sensors remain power-intensive and prone to cross-talk. Optical schemes based on surface plasmons enable remote read-out, but single-metal devices offer either weak H2 affinity or poor plasmonic quality. Here we employ full-wave finite-difference time-domain (FDTD) simulations to map the hydrogen response of nanohole arrays (NAs) that can be mass-produced by colloidal lithography. Square lattices of 200 nm holes etched into 100 nm films of Pd, Mg, Ti, V, or Zr expose an intrinsic trade-off: Pd maintains sharp extraordinary optical transmission modes but shifts by only 28 nm upon hydriding, whereas Mg undergoes a large dielectric transition that extinguishes its resonance. Vertical pairing of a hydride-forming layer with a noble metal plasmonic cap overcomes this limitation. A Mg/Pd bilayer preserves all modes and redshifts by 94 nm, while the predicted optimum Ag (60 nm)/Mg (40 nm) stack delivers a 163 nm shift with an 83 nm linewidth, yielding a figure of merit of 1.96—surpassing the best plasmonic hydrogen sensors reported to date. Continuous-film geometry suppresses mechanical degradation, and the design rules—noble-metal plasmon generator, buried hydride layer, and thickness tuning—are general. This study charts a scalable route to remote, sub-ppm, optical hydrogen sensors compatible with a carbon-neutral energy infrastructure.

Keywords: NAs; plasmonic hydrogen sensors; finite-difference time-domain simulation; extraordinary optical transmission

check for updates

Received: 2 July 2025
Revised: 7 August 2025
Accepted: 14 August 2025
Published: 15 August 2025

Citation: Feng, J.; Liu, Y.; Chen, X.; Cheng, M.; Ai, B. Theoretical Design of Composite Stratified Nanohole Arrays for High-Figure-of-Merit Plasmonic Hydrogen Sensors. *Chemosensors* **2025**, *13*, 309. https://doi.org/10.3390/chemosensors13080309

Copyright: © 2025 by the authors. Licensee MDPI, Basel, Switzerland. This article is an open access article distributed under the terms and conditions of the Creative Commons Attribution (CC BY) license (https://creativecommons.org/licenses/by/4.0/).

1. Introduction

Hydrogen is considered essential for future carbon-neutral energy systems, but its wide flammability range (4–75 vol%) in air and low ignition energy require detectors that are fast, safe, and preferably remote [1]. Conventional sensors—such as semiconducting oxide chemiresistors [2,3], catalytic-combustion sensors [4,5], and electrochemical cells [6,7]—operate at high temperatures, consume significant power, and face issues with cross-sensitivity and safety (details seen in Section S1, Supporting Information (SI)), limiting their use in many applications [7–28]. In contrast, plasmonic hydrogen sensors have emerged as a highly promising technology due to their unique combination of sensitivity, safety, and versatility [29,30]. These sensors operate by monitoring changes in the optical properties of noble-metal nanostructures, most commonly palladium or its alloys, as they interact with hydrogen molecules. Upon hydrogen adsorption and hydride formation, the dielectric function of the metal changes, resulting in a measurable shift

in the surface plasmon resonance (SPR) or localized surface plasmon resonance (LSPR) signal. This enables real-time, label-free detection with sub-ppm sensitivity and rapid response times, often below one second, which surpasses the performance of many conventional sensor types. Optical read-out provides intrinsic safety by eliminating the risk of electrical sparks, making plasmonic sensors particularly suitable for deployment in hazardous or confined environments. Additionally, the remote and distributed sensing capabilities of optical systems allow for flexible integration, including fiber-optic and on-chip configurations. As a result, plasmonic hydrogen sensors are increasingly recognized as an advanced platform for reliable and safe hydrogen monitoring in industrial and environmental applications.

LSPR [31] in noble-metal nanoparticles are highly sensitive to hydrogen, but single-metal nanoparticles cannot combine their strong plasmonic response with high hydrogen affinity. Gold nanoparticles show fast but weak signals due to limited Au–H interactions [32], while palladium offers greater sensitivity [33,34] and magnesium yields larger optical changes but has slow desorption and poor stability [35]. Other hydrogen-active metals like Y, Zr, Ti, and V produce only small spectral shifts [36,37]. Overall, single-metal nanoparticles are limited by single-mode optics, hysteresis, and structural degradation upon cycling, restricting their sensitivity and durability. To overcome these limitations, researchers have created multi-metal nanostructures combining hydrogen-active metals (Pd, Mg) with plasmonically strong metals (Au, Ag), achieving chemical and optical synergy. Structures such as Pd–Au dimers [38], Pd@Au core–shells [39], and alloy nanodisks [40] show improved detection limits (down to 3 ppm), faster response times (as low as 1 s), and enhanced stability. However, these composites still rely on single plasmonic modes and remain structurally fragile. Periodic noble-metal films with sub-wavelength features, known as plasmonic crystals, further advance the field by enabling both LSPR and propagating surface plasmon polaritons (SPPs), which have greater refractive index sensitivity [41]. For example, Pd nanopore arrays and bilayer systems with nanoshells show large optical shifts (up to 200 nm) and faster dynamics [42]. Stretchable devices using Pd nanogrooves on PDMS can further amplify signals and lower detection limits [43]. Nonetheless, the absence of multi-metal chemistry in these films still limits hydrogen uptake and long-term stability.

These studies reveal three essential requirements for next-generation plasmonic hydrogen sensors: (i) strong H_2 chemisorption, (ii) strong and preferably multi-modal plasmonic resonances, and (iii) both structural and chemical robustness. Single-metal nanoparticles cannot meet all these criteria; multi-metal nanoparticles offer chemical–plasmonic synergy but are limited by single-mode optics and poor mechanical stability, while single-metal plasmonic films provide multiple resonances and improved robustness but lack chemical synergy. As a result, no current design fully leverages plasmonic potential for hydrogen sensing. A promising approach is to fabricate ordered micro-/nanostructured films by stacking hydrogen-active and plasmonically strong metals. These stratified systems could combine multi-metal chemistry with LSPR, SPP, and cavity modes, while the continuous-film geometry reduces fragmentation seen in nanoparticles. However, key questions remain about optimal material combinations, layer sequence and thickness, and their impact on optical properties. Resolving these challenges is crucial to achieving plasmonic hydrogen sensors with sub-ppm detection limits, sub-second response times, and long-term stability—critical for the safe and large-scale use of hydrogen in carbon-neutral energy systems.

In this work, we systematically investigate the plasmonic and hydrogen sensing properties of nanohole arrays (NAs) constructed from single metals, binary hydrogen-active metal bilayers, and—critically—hybrid bilayers integrating noble metals (Au, Ag)

with hydride-forming partners (Pd, Mg). By rigorous electromagnetic simulations, we elucidate how the interplay of material composition, stacking sequence, and layer thickness governs the spectral response and figure of merit of these nanostructures. Our results reveal that bilayer NAs capped with Au or Ag effectively decouple plasmon generation from hydrogen transduction, enabling both sharp, trackable resonances and strong hydrogen-induced spectral shifts. Notably, architectures in which Mg or Pd is buried beneath a noble-metal cap achieve an order-of-magnitude improvement in sensing figure of merit compared to their monometallic counterparts, due to the synergistic enhancement of both optical confinement and chemical sensitivity. These findings provide clear design principles for next-generation plasmonic hydrogen sensors, offering sub-ppm detection limits, rapid response, high stability, and compatibility with scalable fabrication—thus paving the way for safe, practical hydrogen monitoring in carbon-neutral energy systems.

2. Methods

FDTD calculation: Finite-difference time-domain (FDTD) simulations were performed using the commercial software package FDTD Solutions (Lumerical Solutions, Inc., Vancouver, BC, Canada) to obtain the $T(\lambda)$ and near-field E-field distributions of the nanohole arrays (NAs). To model an infinite periodic system, a rectangular unit cell was constructed consisting of a central nanohole and four quarter nanoholes at the corners, with periodic boundary conditions applied along both in-plane directions. An automatic non-uniform mesh was employed across the entire simulation domain to ensure high numerical accuracy, with mesh refinement set to conformal variant 1. Frequency-domain field profile monitors were incorporated to record the E-field distributions and $T(\lambda)$ under continuous-wave excitation. The incident E-field amplitude was normalized to unity, enabling quantitative evaluation of electromagnetic field enhancement. Optical constants for Au and Ag were sourced from Palik's Handbook of Optical Constants of Solids. For the "hydrogenated" state, the dielectric functions were taken from Ref. [36], where they were measured after exposure to 1 bar of pure H_2 at room temperature (flow $\approx$ 20 sccm). Hence the simulated spectra corresponded to fully saturated hydrides.

3. Results and Discussion

3.1. Single-Layer NA

The periodic sub-wavelength apertures sustain extraordinary optical transmission (EOT) [44]: incident light couples into SPPs at the metal/dielectric interfaces, traverses the nanoholes, and re-emerges on the opposite side. The resonant coupling produces transmitted intensities far above the geometrical open-area limit, while still obeying overall energy conservation. Because the resonance depends on the local dielectric function, transmission responds acutely to refractive index changes and to hydride formation (MH_x) during hydrogen uptake. The architecture thus offers pronounced optical signal enhancement (EOT), a chemically active surface, mechanical robustness, and full compatibility with scalable, low-cost fabrication. Figure 1a illustrates the nanohole array (NA) conceived for hydrogen sensing. A 100 nm thick monometallic film (Pd, Mg, Ti, V, or Zr) is perforated with a hexagonal lattice of circular holes 200 nm in diameter and 500 nm in pitch on a glass substrate. These geometrical values are selected on the basis of established plasmonic dispersion theory, empirical EOT guidelines, and practical colloidal lithography constraints. For a hexagonal lattice, the in-plane wave vector of the first-order (1,0) Bragg mode is $|G| = \frac{4\pi}{\sqrt{3}\,p}$; inserting the tabulated optical constants of Pd (Re $\varepsilon_m \approx -4$ around 700 nm) and of glass ($\varepsilon_d \approx 2.25$) into the relation $\lambda_{(1,0)} \approx \frac{2\pi}{|G|}\,\mathrm{Re}\left\{\sqrt{\frac{\varepsilon_m \varepsilon_d}{\varepsilon_m+\varepsilon_d}}\right\}$ gives a resonance near 680–730 nm when $p \approx 500$ nm. Positioning the main EOT peak in this visible/NIR window allows the use of inexpensive Si or InGaAs light sources and detectors while keeping Pd absorption

tolerable. The hole diameter is chosen so that $d/p \approx 0.40$. Numerous experimental and numerical studies [45] of EOT arrays have shown that (i) the transmitted intensity scales roughly as $(d/p)^4$ up to $d/p \approx 0.5$, (ii) the resonance linewidth broadens markedly once d/p exceeds ~0.5, and (iii) film integrity deteriorates for $d/p < 0.3$ during hydride-induced lattice expansion. A diameter of 200 nm therefore offers a favorable compromise between optical throughput, Q-factor, reactive surface area, and mechanical robustness. It also matches the size obtained after oxygen-plasma shrinking of standard 500 nm polystyrene spheres, and is a low-cost mask that yields centimeter-scale uniformity based on colloidal lithography (detailed fabrication steps seen in Section S2, Supporting Information (SI)) [41,46,47].

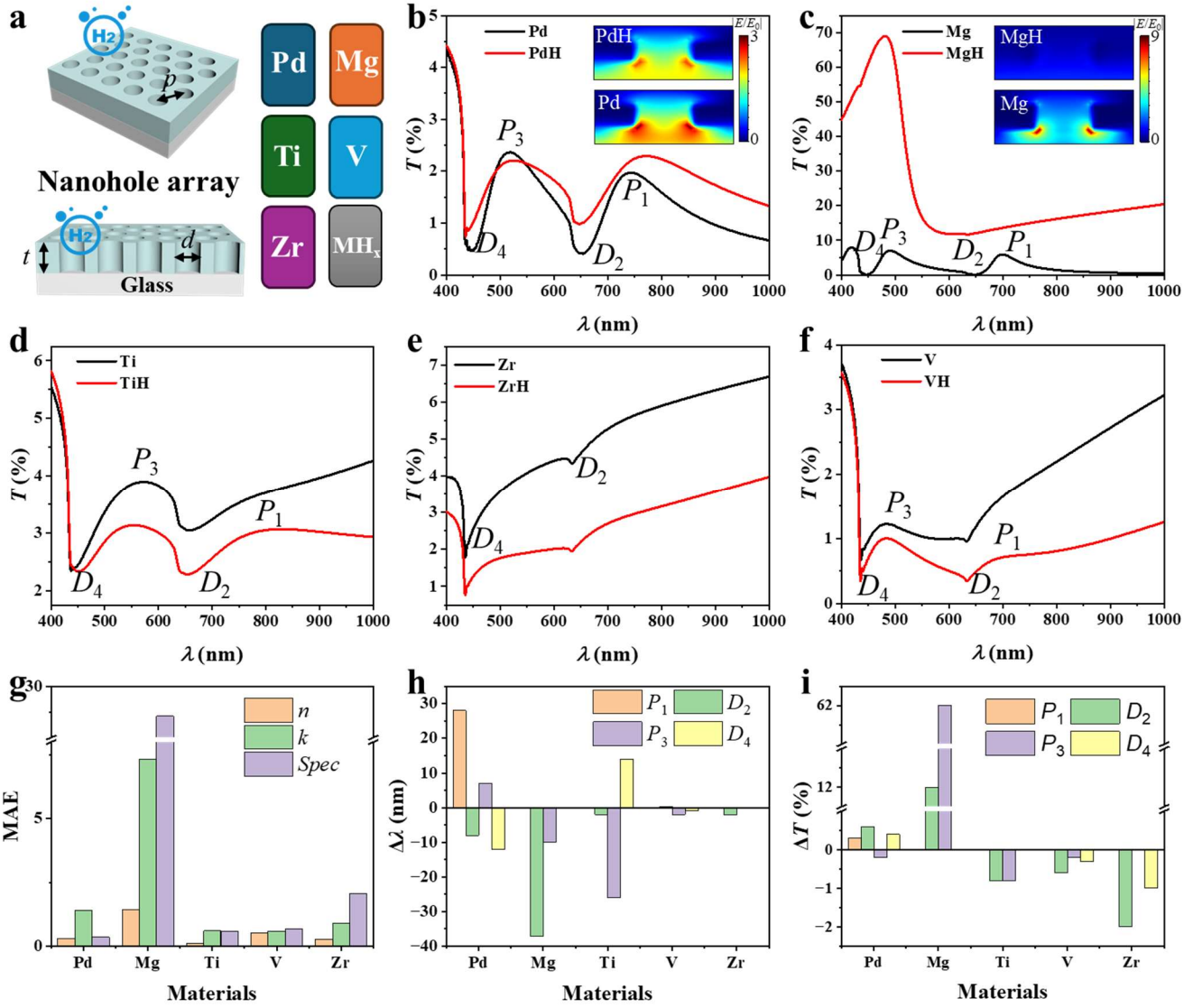


Figure 1. (**a**) Schematic illustration of the monometallic NA architecture and the structural parameters of pitch p, diameter d, and thickness t. Calculated $T(\lambda)$ for NAs of (**b**) Pd, (**c**) Mg, (**d**) Ti, (**e**) Zr, and (**f**) V before (black) and after (red) hydrogenation. Insets in (**b**,**c**) show the E-field intensity maps ($|E/E_0|$) at peak P1. (**g**) MAEs of the real (n) and imaginary (k) parts of the RI upon hydrogenation for each metal, alongside the spectral MAE(Spec). (**h**) Wavelength shifts ($\Delta\lambda$) of the key spectral features (P1, P3, D2, D4) upon hydrogen uptake. (**i**) Transmission changes (ΔT) at these features for each metal.

All optical simulations were conducted in the 400–1000 nm range. This window overlaps the main EOT resonance (≈650–800 nm), matches the detection range of low-cost Si photodiodes and InGaAs arrays, and avoids the stronger intrinsic losses of Pd, Mg, Ti,

V, and Zr at longer wavelengths. A normally incident (θ = 0°) broadband plane wave was used for FDTD simulations; the latter employed the software's default unity field amplitude, as only relative transmittance $T(\lambda)$ was required. Tabulated room-temperature dielectric functions (293 K) were used throughout. We used the main EOT peak shift ($\Delta\lambda_1$), the full width at half maximum (FWHM), and the figure of merit (FoM = $\Delta\lambda_1$/FWHM) as the primary metrics for direct and comprehensive comparison of all samples. To further quantify the sharpness of the resonance, we introduced the signal-to-width ratio (SWR), defined as SWR = $(T_{peak} - T_{base})\%/\text{FWHM}$. This parameter comprehensively reflects both the height and width of the resonance peak, thus providing a more robust assessment of the peak sharpness.

Pd, Mg, Ti, V, and Zr were chosen for their ability to absorb hydrogen and their distinct plasmonic figures of merit [36]. Figure 1b–f present FDTD-calculated normal-incidence transmission spectra $T(\lambda)$ for each metal; the corresponding optical constants before and after hydrogenation are obtained from a previous report [36], and were measured for fully saturated hydrides. Black and red curves denote the pristine and hydrogenated states, respectively. For Pd (Figure 1b) and Mg (Figure 1c) four prominent features appear: two transmission maxima (P1, P3) and two minima (D2, D4). P1 corresponds to the (1, 0) SPP at the glass/metal interface [48], whereas P3 arises from overlap of the (1, 1) and (1, 0) SPP at the glass/metal and air/metal interfaces [47], respectively. D2 and D4 coincide with Wood's anomalies [49] where diffracted orders graze the array plane, redistributing optical energy and suppressing transmission. The Mg array exhibits a markedly stronger EOT response: P1 reaches 5.8% transmission and 0.084 SWR versus 2.0% and 0.01 for Pd. Electric field maps at P1 (insets, Figure 1b,c) reveal average $|E/E_0|$ values of 1.88 (Mg) and 1.00 (Pd), with the field largely confined to the glass side. Mg's superiority stems from its lower intrinsic losses (smaller Imε) and higher plasma frequency, which together enable more efficient, less damped SPP excitation and sharper resonances. NAs of Ti, Zr, and V (Figure 1d–f) display broader, weaker EOT signatures, reflecting higher optical losses and less favorable dielectric functions. Overall, plasmonic performance follows the qualitative order Mg > Pd > Zr ≈ V ≈ Ti [50,51].

Hydrogen uptake (red curves in Figure 1b–f) markedly alters the $T(\lambda)$ of every NA, a direct consequence of the modified complex permittivity of the corresponding hydrides. The extent and nature of these spectral changes depend strongly on the parent metal. Mg provides the most striking example: conversion of metallic Mg to dielectric MgH_2 suppresses SPP excitation, causing the dominant EOT resonance P1 to vanish and the average near-field amplitude $|E/E_0|$ in the glass to fall from 1.88 to 0.75. The concomitant spectral shift and peak attenuation yield an unambiguous optical signature, but the metal-to-insulator transition renders the response largely binary and only partially reversible. Pd behaves quite differently. Hydride formation perturbs, yet does not extinguish, its metallic character, so the P1 resonance is preserved while its position and intensity change smoothly; the associated near-field amplitude only decreases to 0.92. Because this resonance remains traceable throughout repeated hydrogen cycling, Pd NAs afford reversible and quantitative hydrogen detection. Ti, V, and Zr occupy an intermediate regime. Their intrinsic plasmonic quality is compromised by large ohmic losses, and hydrogenation further broadens or erases the already weak EOT features. As a result, the P1 peak becomes indistinct or disappears, limiting the achievable sensing figure of merit (FoM), although the exceptional chemical robustness of these refractory metals may still justify their use in harsh environments. The primary performance metrics for the single-layer NAs are summarized in Table S2, Supporting Information (SI). Among all samples, only the Pd NA exhibits a measurable response, with an FoM of 0.13.

To elucidate the origin of the material-specific optical responses, we determined the mean absolute errors (MAEs) of the real (n) and imaginary (k) parts of the refractive index (RI) across the visible–near-infrared range and introduced a spectral MAE(Spec) that represented the average absolute difference between the entire $T(\lambda)$ before and after hydrogenation (Figure 1g). Details of the calculation of MAE are shown in Section S4, Supporting Information (SI). Mg exhibits the largest dielectric contrast of MAE(n) = 1.43 and MAE(k) = 7.33, yielding an exceptional MAE(Spec) of 28.84 and confirming the collapse of its plasmonic resonances once metallic Mg converts to dielectric MgH_2. Ti, V, and Zr follow the same positive correlation—relatively small MAE(n) (<0.60) and MAE(k) (<1.00) lead to modest Spec values of 0.59, 0.67, and 2.07, respectively—consistent with the limited modification of their EOT features. Pd constitutes the lone exception. Although hydrogenation of Pd produces appreciable changes in its optical constants (MAE(n) = 0.31, MAE(k) = 1.41), the MAE(Spec) remains an order of magnitude lower (0.36) than that of Ti, V, and Zr. This muted global response arises because the well-defined surface plasmon polariton modes sustained by Pd NAs absorb dielectric perturbations mainly through local wavelength and amplitude adjustments, while partial cancelation between n and k further suppresses overall spectral modulation.

Based on the quantitative data for peak wavelength shifts ($\Delta\lambda$) (Figure 1h) and transmission changes (ΔT) (Figure 1i) upon hydrogenation, several important trends emerge. After hydrogenation, Pd is the only metal in which all four resonances remain discernible. The peak P1 red-shifts by 28 nm and brightens by 0.3%, the peak P3 red-shifts by 7 nm while attenuating by 0.2%, and the Wood anomalies (D2 and D4) move by -8 and -12 nm, respectively, with sub-percent-intensity changes. These modest variations underscore the resilience of Pd plasmonics to hydrogen loading. The response of Mg is diametrically opposed. Formation of MgH_2 suppresses the (1, 0) SPP and the higher-order Wood mode altogether, either through increased damping or by shifting them beyond the measurement window. The surviving Wood anomaly (D2) and hybrid SPP (P3) undergo pronounced blue-shifts of -37 and -10 nm and exhibit dramatic intensity increases of 12% and 62%, respectively, mirroring the drastic alteration of Mg's dielectric function. For Ti, V, and Zr, the already weak plasmonic features in the metallic state become indistinct after hydrogenation; the residual modes display only minor wavelength shifts ($\pm$26 nm) and small, predominantly negative, intensity variations ($\leq$2%), consistent with the limited changes in their optical constants. Collectively, the data establishes a clear hierarchy. Large dielectric perturbations, exemplified by Mg, can extinguish or strongly amplify individual SPP or Wood modes; moderate perturbations, typified by Pd, mainly induce wavelength shifts with minimal amplitude variation; and negligible perturbations, characteristic of Ti, V, and Zr, leave the transmission landscape largely unaltered.

3.2. Bilayer NA Composed of Pd, Mg, Ti, V, and Zr

As demonstrated in Figure 1, no single metal simultaneously delivers large signal amplitudes and well-defined resonances, so a new structural concept is required. We therefore investigated vertical bilayers in which two hydrogen-active metals are stacked in a single nanohole film. Systematic exploration of all ten binary combinations of Pd, Mg, Ti, V, and Zr was undertaken to identify synergistic configurations that transcended the intrinsic trade-offs of monometallic sensors. Figure 2 presents the calculated $T(\lambda)$ for each bilayer before (solid curves) and after (dashed curves) hydrogenation. The total t is 100 nm with each material layer of 50 nm. The p and d are the same as those in Figure 1. In the notation "A/B", A denotes the air-facing layer and B the glass-facing layer; both stacking orders for every metal pair are shown in the same panel, with color-coded curves corresponding to specific arrangements as indicated in the legend.

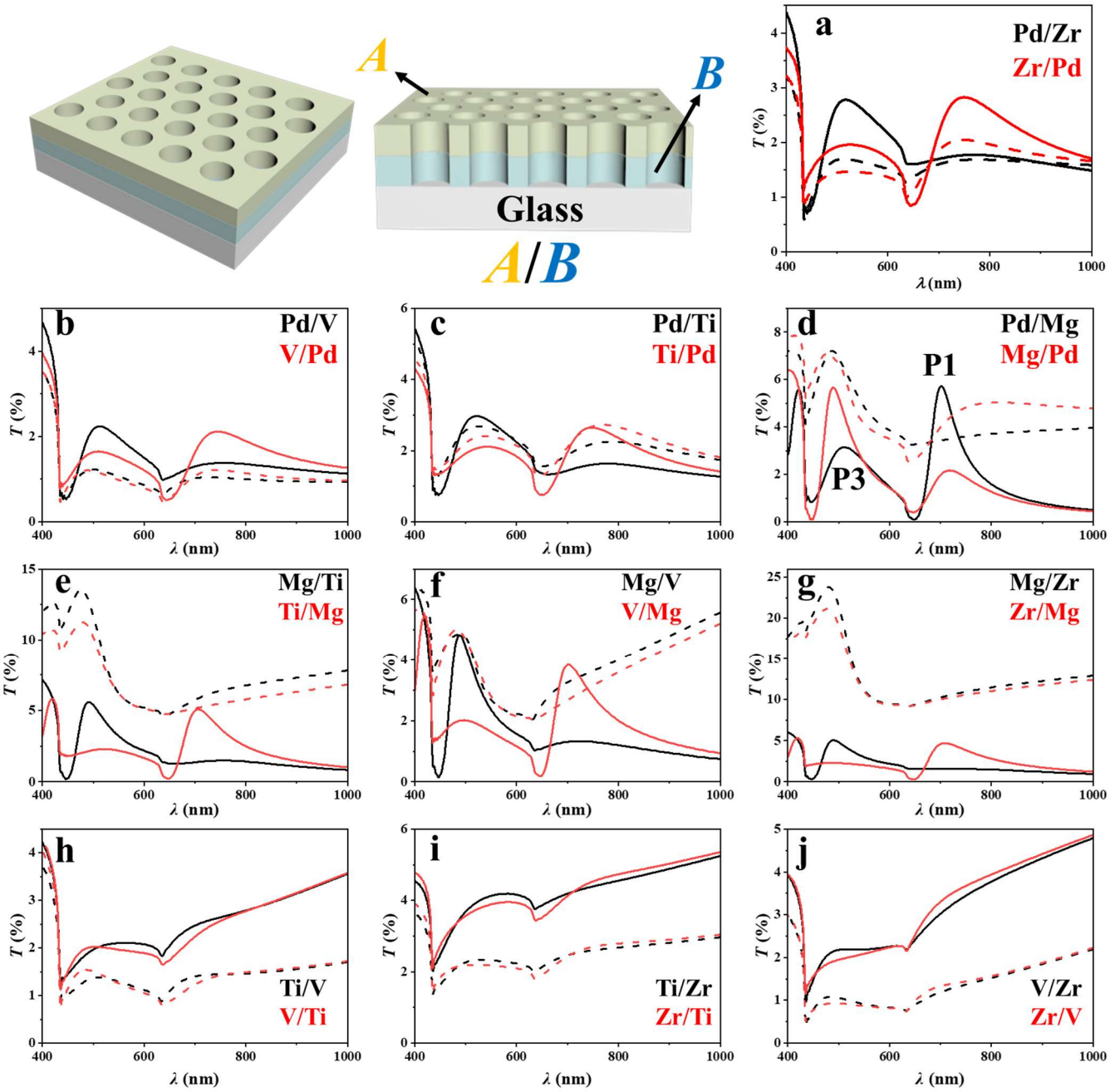


Figure 2. (**a**–**j**) FDTD-calculated $T(\lambda)$ for all ten bilayer NAs composed of Pd, Mg, Ti, V, and Zr, shown before (solid curves) and after (dashed curves) hydrogenation. The top-left panel shows the structure of the bilayer NAs. In the "A/B" notation, A is the air-facing layer and B is the glass-facing layer; both stacking orders for each metal pair are shown in each panel, with color-coded curves as indicated.

Whenever the plasmonically stronger component—Pd or Mg—is placed on top (Figure 2a–g), the resonance associated with the air/metal interface (P3) dominates. Reversing the order shifts optical weight to the glass/metal interface so that P1 becomes the most intense peak. This sensitivity to layer sequence is negligible in Ti/V/Zr bilayers (Figure 2h–j) because their intrinsic plasmonic quality factors are too low for the interface position to influence resonance strength appreciably. A second salient observation is that bilayers incorporating Pd or Mg retain the full quartet of characteristic features—two EOT maxima (P1, P3) and two Wood anomaly minima (D2, D4)—whereas bilayers composed solely of the weaker plasmonic metals (Ti, V, Zr) exhibit attenuated or missing resonances. These results confirm that the judicious pairing and ordering of dissimilar metals can pre-

serve well-defined tracking features while simultaneously amplifying hydrogen-induced spectral contrast, thereby establishing bilayer NAs as promising platforms for highly sensitive, selective, and durable optical hydrogen sensors.

Electric field (*E*-field) ($|E/E_0|$) maps were calculated for the pristine Pd/Mg and Mg/Pd nanohole bilayers at the two dominant resonances, P1 and P3. In Pd/Mg, P1 is governed by the SPP at the glass/Mg interface; the associated field is strongly confined to this boundary and is far more intense than the field at P3, which is centered at the air/Pd interface. The large field enhancement arises because the bottom Mg layer, having the higher plasmonic quality factor, couples efficiently to the high-index glass substrate. Consequently, P1 outshines P3 in both amplitude and definition. Reversing the layer order equalizes the field distribution. In Mg/Pd the field contrast between the Mg/air and Pd/glass interfaces at P1 is much smaller, whereas the field strength at P3 approaches that at P1. Here the superior plasmonic performance of the top Mg layer compensates for the absence of the glass substrate, while the lower plasmonic quality of the Pd bottom layer partly offsets the benefit of the high-index glass. As a result, P3 becomes the dominant peak, and the relative intensities of P1 and P3 swap compared to the Pd/Mg architecture. In quantitative terms, $|E/E_0| - \mathrm{P1(Pd/Mg)} > |E/E_0| - \mathrm{P1(Mg/Pd)}$, whereas $|E/E_0| - \mathrm{P3(Pd/Mg)} < |E/E_0| - \mathrm{P3(Mg/Pd)}$, fully consistent with the experimentally observed peak intensities.

Hydrogen uptake alters these trends in a systematic way. In every bilayer containing Pd or Mg (Figure 2a–g) the resonances broaden and lose contrast, reflecting increased damping and the modified dielectric functions of the hydrides. Peak degradation is most severe in Mg-based systems because the metal-to-insulator transition of MgH_2 suppresses SPP excitation; nevertheless, comparable, though less dramatic, broadening is also evident in Pd-containing films. Notably, in the Pd/Mg stack, P1 becomes so diffuse that it can no longer be distinguished, whereas in Mg/Pd, a discernible P1 survives. This behavior is readily explained by the RI environment of the plasmonic layer that remains metallic after hydrogenation, namely PdH_x. In Pd/Mg the PdH_x layer is bounded by air and MgH_2 ($n \approx 1.7$); in Mg/Pd it is sandwiched between glass ($n \approx 1.5$) and MgH_2. The higher average RI surrounding PdH_x in the Mg/Pd geometry enhances field confinement (Figure 3), thereby preserving the visibility of P1. For Pd/Mg the lower effective index, combined with additional damping in the adjacent MgH_2, weakens field localization and erases the peak. In the hydrogenated Pd/Mg film the remaining strong field is therefore found at P3, making this the dominant resonance. In summary, before hydrogenation, the field concentrates at the Mg interface because Mg exhibits a stronger plasmonic response; after hydrogenation the field migrates to the PdH_x interface, whose SPR now dominates. The interchange of field localization between the two interfaces underpins the observed inversion and broadening of the P1 and P3 resonances and highlights the critical roles of layer sequence and dielectric environment in tailoring the optical response of plasmonic hydrogen sensors.

Detailed inspection of the $T(\lambda)$ discloses metal-dependent trends in resonance intensity after hydrogen uptake. In Pd-based bilayers (Figure 2a–d), the response is heterogeneous: some resonances brighten, whereas others fade. This behavior stems from the moderate yet mode-specific change in Pd's complex permittivity upon formation of PdH_x. Hydrogen absorption slightly lowers the extinction coefficient k and shifts the dispersion of SPPs. Resonances whose fields are localized at interfaces that benefit from the reduced damping intensify, while those that are detuned from optimal coupling or suffer diminished field overlap attenuate. Bilayers containing Mg (Figure 2d–g) show a uniformly positive intensity change. The metal-to-insulator transition of MgH_2 removes free carriers, suppresses absorption, and elevates the overall transmission background. Although the resulting

dielectric layer weakens SPP support, the diminished optical loss produces a net enhancement of every spectral feature, rendering the EOT peaks broader but more intense. For stacks composed solely of Ti, V, or Zr, hydrogenation consistently diminishes resonance amplitudes. Their hydrides introduce appreciable damping while offering only marginal shifts in the real RI. The attendant increase in k broadens the already weak EOT and SPP modes, often pushing them below the detection threshold.

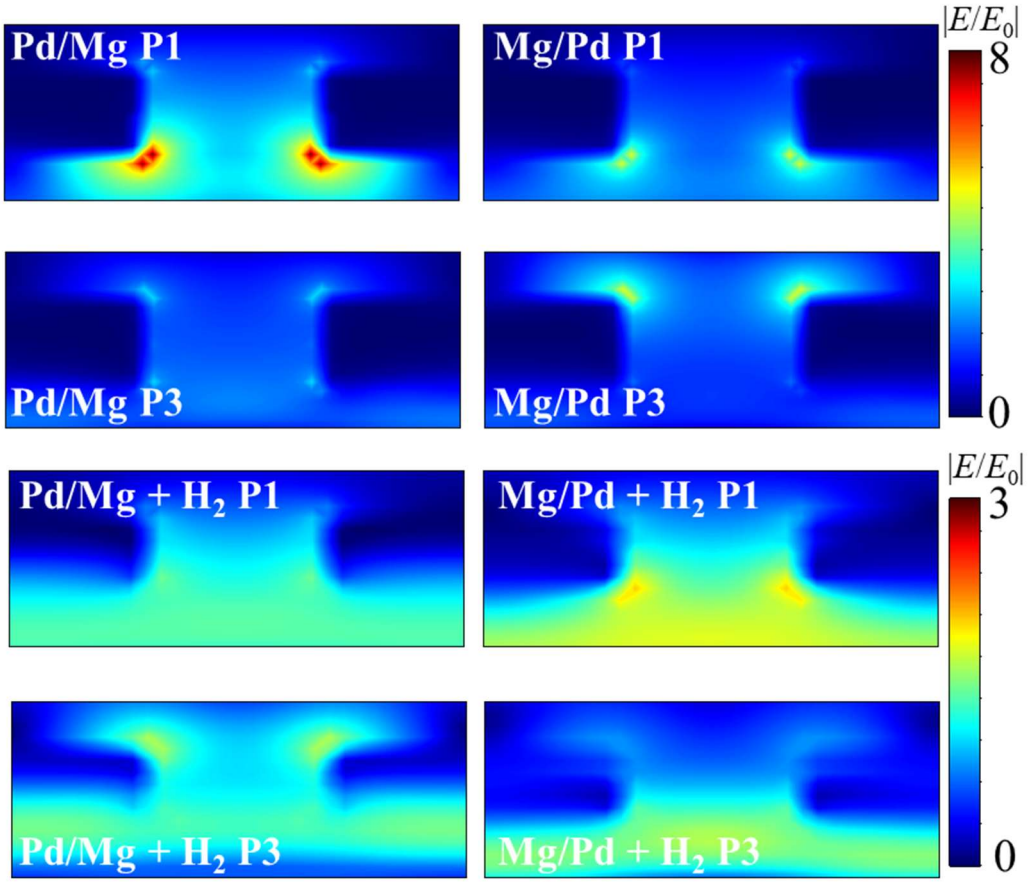


Figure 3. Simulated E-field intensity ($|E/E_0|$) maps at the main resonances (P1, P3) for pristine and hydrogenated Pd/Mg and Mg/Pd bilayers.

Figure 4a,b summarize the hydrogen-induced wavelength shifts ($\Delta\lambda$, nm) and transmission variations (ΔT, %) for the ten possible bilayer NAs fabricated from Pd, Mg, Ti, V, and Zr, each examined in both stacking sequences. All numerical values are reported with a single significant digit; "0" therefore indicates a change below 0.5 nm in wavelength and 0.5% in transmission, whereas a slash (/) denotes a resonance that cannot be distinguished after hydrogenation because it merges with the background. The primary performance metrics of the FWHM and FoM of peak P1 are summarized in Table S2, Supporting Information (SI). Among all samples, only the Pd NA exhibits a measurable response, with an FoM of 0.13. The most pronounced response is obtained for the Mg/Pd architecture. Hydrogen absorption red-shifts the peak P1 by $\Delta\lambda_1$ = 94 nm and raises its peak transmission by ΔT_1 = 3%. These variations exceed those of a monometallic Pd array (28 nm, 0.3%) and those of pristine Mg (maximum shift −37 nm), underscoring the synergistic benefit of combining the two metals. The magnitude of $\Delta\lambda$ can be approximated by first-order perturbation theory [52,53],

$$\Delta\lambda \simeq \lambda_0 \, (\Delta n_{\mathrm{eff}}/n_{\mathrm{eff}}), \quad (1)$$

where λ_0 is the original resonance wavelength and n_{eff} is the effective modal index. For Mg, conversion to MgH_2 lowers the real part of the permittivity by $\Delta n \approx -1.4$ at 700 nm while simultaneously reducing optical losses. Substituting this value into Equation (1) yields a predicted red-shift on the order of 90 nm, in quantitative agreement with FDTD simulation. In the inverted Pd/Mg stack the same P1 resonance vanishes entirely because MgH_2 eliminates the metallic boundary at the glass side; however, the high-order hybrid mode P3 still blue-shifts by −22 nm, confirming that a measurable spectral response is maintained, albeit redistributed among the surviving modes.

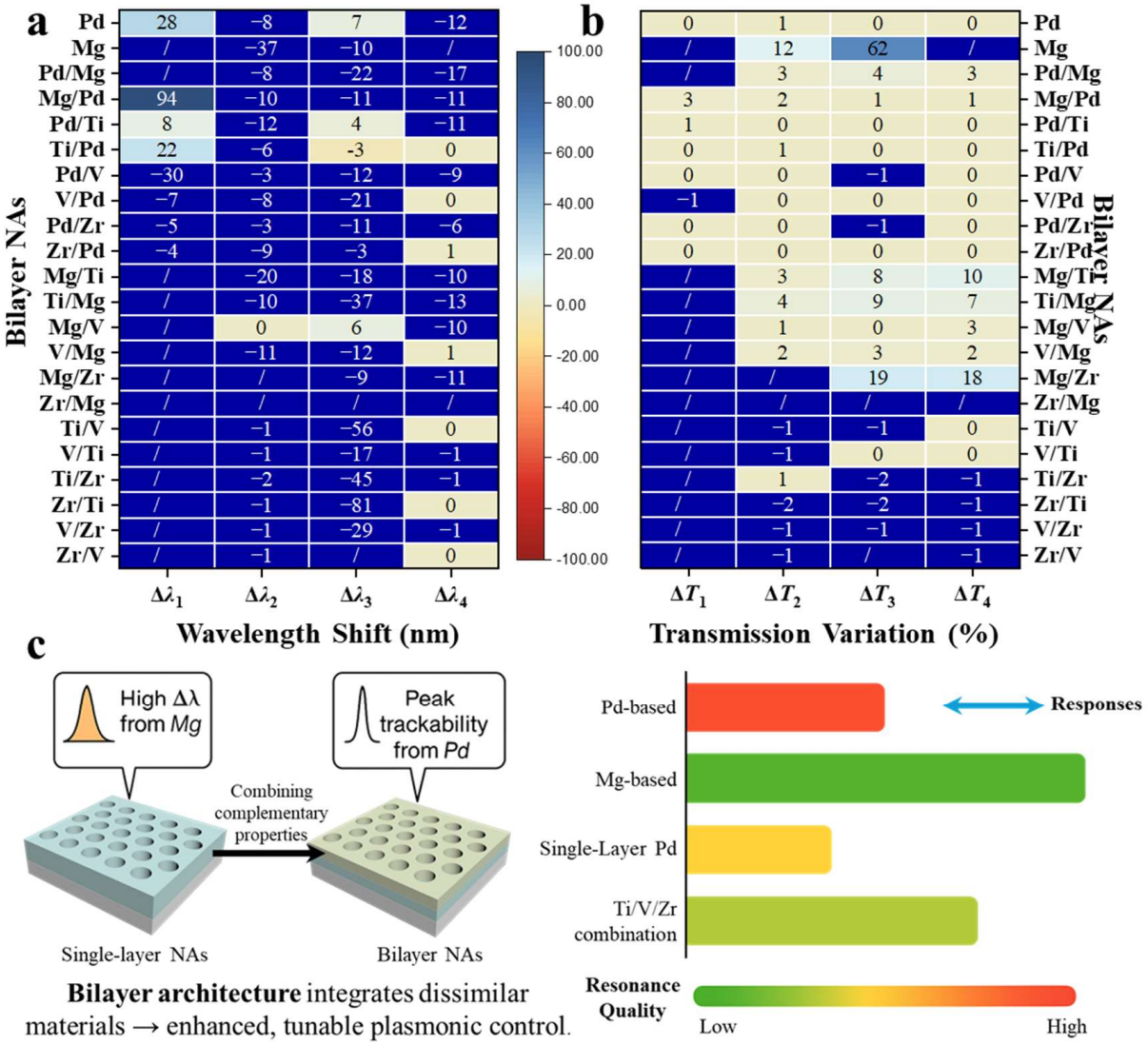


Figure 4. Heating map of (**a**) hydrogen-induced peak/dip wavelength shifts ($\Delta\lambda$) and (**b**) transmission variation (ΔT) for the ten possible bilayer combinations of Pd, Mg, Ti, V, and Zr NAs, each tested in both stacking sequences (A/B: A = air side, B = glass side). A "0" indicates a change below 0.5 nm in wavelength and 0.5% in transmission, and "/" denotes peaks indistinguishable after hydrogenation. (**c**) Schematic summary of the main trends.

Bilayers that combine Pd with Ti, V, or Zr respond far more modestly. For Pd/Ti, for example, P1 moves by only 8–22 nm with $\Delta T_1 \leq 1\%$. Pd/V, V/Pd, Pd/Zr, and Zr/Pd even show slight blue-shifts (−4 nm to −30 nm) accompanied by negligible intensity changes. These muted signals mirror the small perturbations of the dielectric functions of TiH_x, VH_x, and ZrH_x ($|\Delta\varepsilon| < 0.2$) and the concomitant increase in damping [54]. When Mg is paired with Ti, V, or Zr, hydrogenation again removes the P1 resonance, yet the remaining peaks

still profit from Mg's large $|\Delta n|$. The hybrid P3 mode blue-shifts by up to −37 nm and the background transmission rises by as much as 19%. Although these absolute changes surpass those of the corresponding Pd-free bilayers, the absence of a trackable P1 peak reduces the FoM = $|\Delta\lambda|$/FWHM (full width at half maximum) to below unity, limiting practical sensing accuracy. Combinations consisting solely of weak plasmonic metals (Ti, V, Zr) perform poorly. Most resonances cannot be located after hydrogen exposure, and those that do survive present Wood's anomaly shifts no greater than 2 nm with $\Delta T \leq 2\%$. While the broad hybrid P3 peak can move up to −81 nm, its full width at half maximum (≈150 nm) suppresses the FoM to <0.5, revealing the inability of these metals to sustain low-loss SPPs.

The conclusion of our systematic comparison of bilayer NAs is depicted in Figure 4c. Bilayers incorporating Pd and/or Mg deliver the most pronounced hydrogen responses—exemplified by the Mg/Pd configuration, whose (1, 0) glass-side SPP (P1) red-shifts by 94 nm and gains 3% in transmission, far surpassing the 28 nm/0.3% response of monometallic Pd and the −37 nm shift in pure Mg. Apart from the hydrogenated Pd/Mg stack, which loses its P1 resonance, Pd-based bilayers retain the full complement of EOT peaks and Wood anomalies throughout hydrogen cycling, thereby preserving trackability. In contrast, Ti, V, and Zr pairings exhibit minimal or negative wavelength shifts, severe broadening, and, in many cases, unresolvable features, underscoring their limited utility for sensing. Although stacking order can fine-tune individual modes, the choice of metals overwhelmingly determines both the magnitude and sign of $\Delta\lambda$ and ΔT; integrating dissimilar layers thus offers clear advantages over single-metal films. Nevertheless, hydride-induced damping broadens even the best resonances, restricting the FoM and highlighting the need for further engineering—such as integration with strong SPR materials—to fully exploit bilayer architectures in high-precision plasmonic hydrogen sensors.

3.3. Bilayer NAs with Au and Ag

Figure 5 presents the $T(\lambda)$ for NAs incorporating Pd and Mg layers in combination with Au and Ag. The investigated configurations include Pd/Au, Au/Pd, Pd/Ag, Ag/Pd, Mg/Ag, Ag/Mg, Mg/Au, and Au/Mg, where the material listed after the "/" denotes the bottom (glass-facing) layer. The total t is 100 nm with each material layer of 50 nm. The p and d are the same as those in Figure 1. Other than Ti, V, and Zr, Pd and Mg are selected because their conversion to PdH_x or MgH_2 alters the real and imaginary parts of the dielectric function by $|\Delta n| \approx 0.3$ and 1.4, respectively, thereby red- or blue-shifting SPP modes. Au and Ag, in contrast, scarcely absorb hydrogen yet sustain high-quality SPPs (Imp $\varepsilon_{Au,Ag} \ll$ Im $\varepsilon_{Pd,Mg}$), so that introducing them should sharpen the spectra without compromising chemical sensitivity. The (1, 0) SPP resonance mode at the glass/upper-metal interface (P1, λ_1) is chosen for quantitative evaluation because it is spectrally prominent, highly sensitive to dielectric changes from hydrogen absorption, and enables reliable comparison of sensor performance. The pristine spectra (Figure 5, solid curves) confirm that integrating Au or Ag dramatically narrows peak P1; linewidths decrease from 180–240 nm (①②) for Pd/Mg to 40–60 nm for Au- or Ag-containing stacks (③–⑩) because of the lower ohmic damping of noble metals. Sharpening is most pronounced when Au or Ag is adjacent to the glass substrate (③⑤⑦⑨), where the high RI ($n \approx 1.5$) strengthens the in-plane wave vector. Field-mapping (Figure 6a) corroborates this trend: the average E-field at resonance is 2.41 for Pd/Ag but only 1.31 for Ag/Pd (4.39 for Mg/Ag and 1.56 for Ag/Mg), reflecting the superior glass/Au (Ag) coupling.

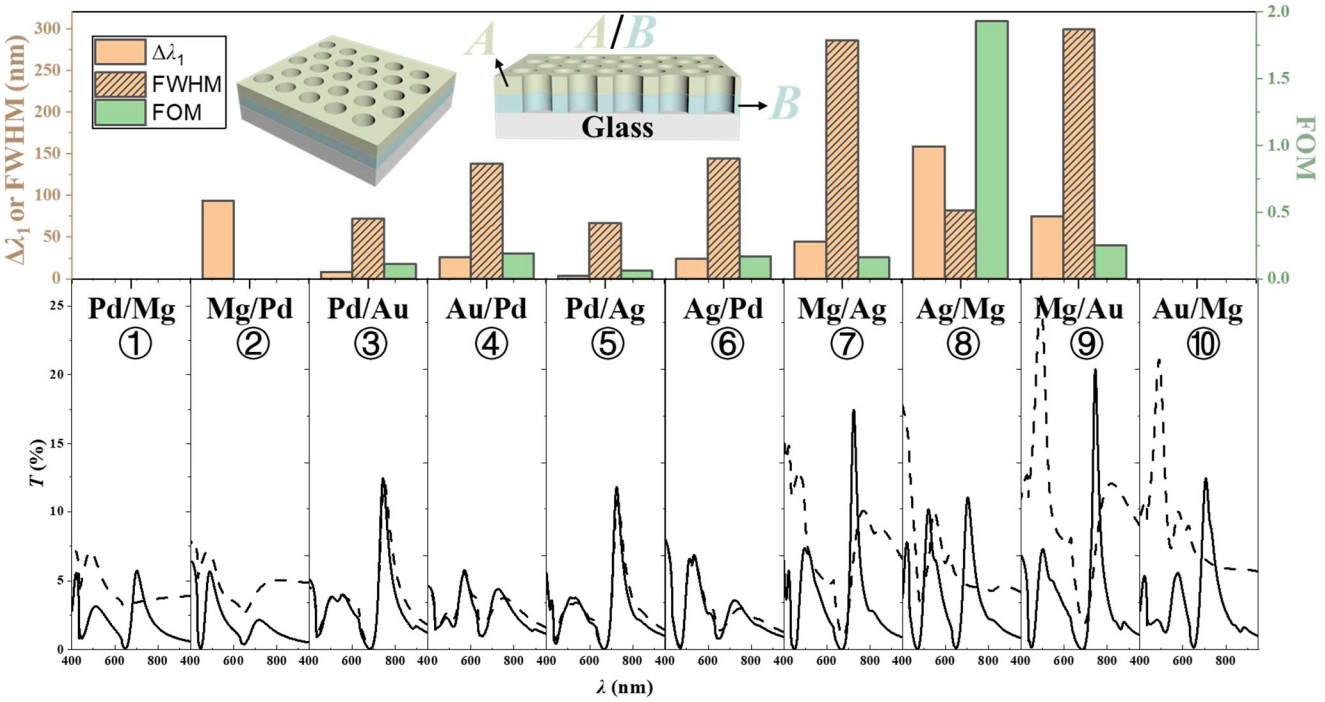


Figure 5. Comparison of $\Delta\lambda_1$ and FWHM (left axis) and FoM (right axis) for the peak P1 in pristine and hydrogenated bilayer NAs composed of Pd or Mg with Au or Ag in both stacking orders. The inset shows the structure of the bilayer NAs. In the "A/B" notation, A is the air-facing layer and B is the glass-facing layer.

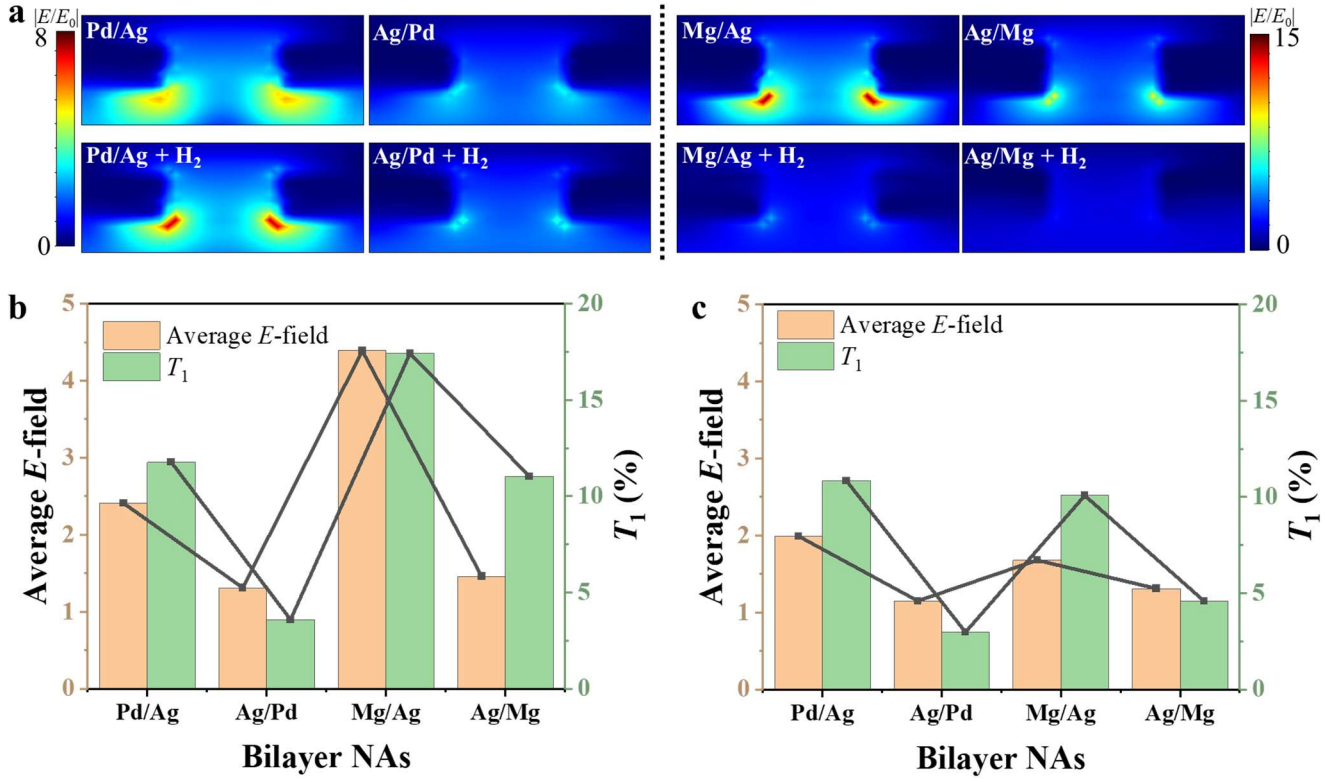


Figure 6. (**a**) Calculated E-field intensity maps ($|E/E_0|$) at P1 for selected bilayer stacks before and after hydrogenation. Average E-field and T_1 at P1 (**b**) before and (**c**) after H_2 exposure.

Upon hydrogen exposure (Figure 5, dashed curves), P1 survives in every Au- and Ag-based architecture except Au/Mg, whereas it vanishes in Pd/Mg (①) and broadens

beyond quantitative evaluation in Mg/Pd (②). The persistence of P1 arises because the electromagnetic energy is still dominated by the noble-metal layer; the accompanying $\Delta\lambda_1$ is nevertheless sensitive to hydride formation in the partner metal. *E*-field maps support this interpretation: the average $|E/E_0|$ at resonance rises to 1.15–1.99 for hydrogenated Ag-based stacks (Figure 6a), whereas it reaches only 1.03 for hydrogenated Pd/Mg (Figure 3). Mg-containing stacks show both the largest shifts ($\Delta\lambda_1$ = 159 nm) and the broadest peaks (FWHM > 250 nm) because the metal-to-insulator transition of MgH_2 simultaneously modifies n_{eff} and increases radiative damping. The calculated FoMs cluster around 0.1–0.2 for Au- and Ag-based architecture, significantly higher than the Pd/Mg and Mg/Pd references, whose P1 is either lost (①) or too diffuse to analyze (②). The Ag/Mg configuration stands out with FoM = 1.94, owing to a large shift of 159 nm combined with a linewidth of only 82 nm. When Au or Ag forms the top layer (④⑥⑧), its evanescent field extends into the PdH_x or MgH_2 over a distance [54], resulting in larger resonance shifts compared to the inverted geometry (③⑤⑦). In the latter case, the field is predominantly confined within the glass substrate, as glass possesses a higher RI than either PdH_x or MgH_2. As illustrated in Figure 6a, the *E*-field in the Pd(Mg)/Ag + H_2 configuration is largely localized within the glass, whereas the Ag/Pd(Mg) + H_2 structure exhibits a more uniform *E*-field distribution across the top air interface, the bottom Mg edge, and the underlying glass. The enhanced resonance at the metal/glass interface, however, leads to a smaller FWHM in models where Au or Ag forms the bottom layer (③⑤ compared to ④⑥, respectively). As a result, the Au/Mg configuration loses the P1 peak (⑩), which can be attributed to both the specific layer arrangement and the inherently weaker SPR of Au compared to Ag.

Furthermore, Au-based stacks exhibit slightly larger resonance shifts than their Ag-based counterparts (③④⑨ compared to ⑤⑥⑦, respectively). The reduced sensitivity of Ag-based stacks originates from the much larger magnitude of the real permittivity of Ag: visible $|\varepsilon'_{\text{Ag}}|$ is roughly two to three times $|\varepsilon'_{\text{Au}}|$, which confines the SPP more tightly to the Ag surface and shortens the decay length into Pd. Because the wavelength sensitivity of an SPP is proportional to $\partial\lambda/\partial\varepsilon_{\text{eff}}$ and this derivative increases as $|\varepsilon'|$ decreases, Au—despite its slightly higher ohmic loss—permits deeper field penetration, a larger overlap with the hydride layer, and therefore a greater resonance displacement for the same change in dielectric function. In addition, Figure 6b,c plot the average *E*-field based on Figure 6a and the transmission intensity at the P1 mode for Ag + Mg before and after exposure to H_2, respectively; the two traces evolve in parallel with the P1 transmission amplitudes, demonstrating that the change in resonance intensity is directly proportional to the local field enhancement sustained by the structure. These results demonstrate that integrating a non-reactive, low-loss plasmonic layer with a hydride-forming partner decouples chemical transduction from optical losses, thereby enhancing peak definition and substantially improving the FoM—a prerequisite for high-precision plasmonic hydrogen sensing.

The influence of the thickness ratio between the active, hydride-forming metal (Pd or Mg) and the plasmonic cap (Au or Ag) was evaluated by keeping the total metallic thickness fixed at 100 nm and gradually transferring thickness from one layer to the other. Figure 7a–c summarize the hydrogen-induced $\Delta\lambda_1$, FWHM, and FoM for every combination of Pd/Au, Au/Pd, Pd/Ag, Ag/Pd, Mg/Au, Au/Mg, Mg/Ag, and Ag/Mg NAs; on each abscissa the plotted thickness refers to the material highlighted in the legend: the complementary layer completing the 100 nm stack. For Pd-Au bilayers the stacking sequence dictates the field distribution and therefore the sensing behavior. When Pd lies on top of Au (Pd/Au) the resonance shift rises from 3 nm at 5 nm Pd to 39 nm at 90 nm Pd, reflecting the larger hydride volume directly exposed to hydrogen. At the same time, the peak broadens from 43 nm to 163 nm because the increased optical damping of thick Pd degrades the quality factor, so FoM improves only marginally from 0.07 to 0.24. For Pd/Au structures, $\Delta\lambda_1$

and FWHM increase slowly when the Pd layer is thinner than 60 nm but rise rapidly as thickness exceeds this value. This is because a thin Pd layer confines the *E*-field mainly within the glass substrate, limiting its effect on the top interface. As the Pd layer becomes thicker, it significantly alters the RI at the surface, shifting the *E*-field toward the PdH layer and resulting in a marked increase in $\Delta\lambda_1$ and FWHM.

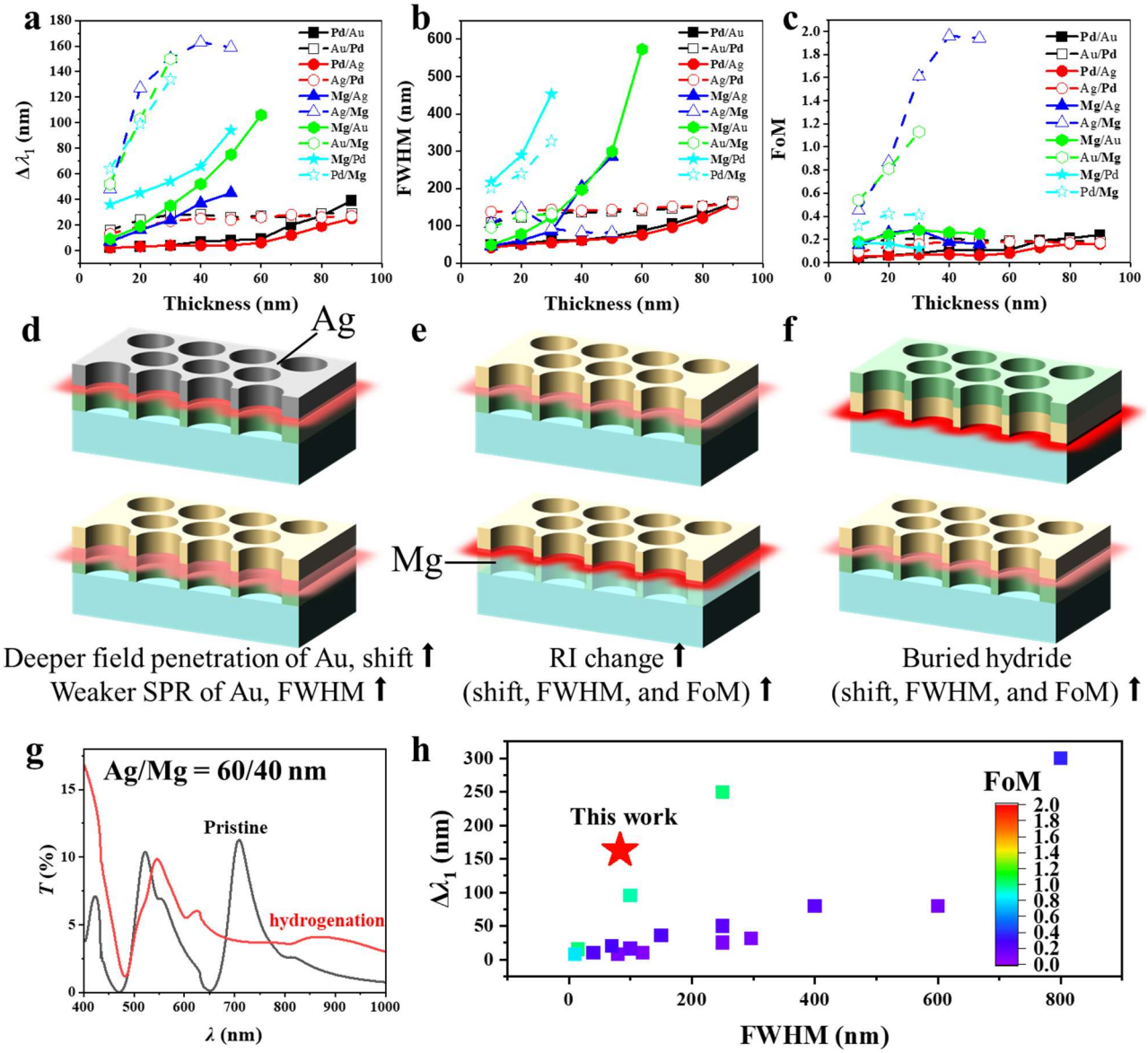


Figure 7. (**a**) $\Delta\lambda_1$, (**b**) FWHM, and (**c**) FoM for Pd/Au, Au/Pd, Pd/Ag, Ag/Pd, Mg/Au, Au/Mg, Mg/Ag, and Ag/Mg NAs, as a function of the thickness of the hydride-forming metal (Pd or Mg, abscissa; total thickness = 100 nm). (**d**–**f**) Representative configurations showing different combinations of capping and hydride-forming layers, with the red arrows indicating the enhanced *E*-field distribution at the metal/hydride or metal/glass interfaces. (**g**) *T* of Ag/Mg (60 nm/40 nm) bilayer before and after hydrogenation. (**h**) Plot of state-of-the-art plasmonic hydrogen sensors, plotting maximum $\Delta\lambda$, FWHM, and FoM. The FoM values are indicated by the color bar.

Reversing the sequence (Au/Pd) relocates the SPP to the air/Au interface and lets its evanescent tail probe the underlying Pd. The $\Delta\lambda_1$ and FWHM increase rapidly as Pd thickness increases up to 30 nm, and then stabilize at greater thicknesses. For Au/Pd, even a few nanometers of Pd fall within the field maximum; consequently, $\Delta\lambda_1$ already jumps to 46 nm at 20 nm Pd, thereafter saturating, whereas the linewidth stabilizes near 170 nm. The

penetration depth that governs this behavior is $\delta \approx \frac{\lambda}{2\pi\sqrt{|\varepsilon'(\mathrm{Au})|}} \approx 25$ nm at $\lambda \approx 700$ nm [54], so Pd thicker than $\approx\delta$ no longer alters the modal energy distribution. The counter-acting trends in shift and broadening leave FoM essentially constant around 0.20. Replacing Au with Ag preserves the qualitative picture but lowers the overall sensitivity. With Pd on top of Ag (Pd/Ag), $\Delta\lambda_1$ grows from 2 nm to 25 nm while FWHM inflates from 41 nm to 164 nm, keeping the FoM below 0.16. Placing Ag on top (Ag/Pd) increases $\Delta\lambda_1$ slightly to 28 nm for 70 nm Pd, but also widens the peak (FWHM = 171 nm), so FoM hovers between 0.14 and 0.21. The inferior response compared to the Au-capped stacks originates from the deeper field penetration of Au, a larger overlap with the hydride layer, and therefore a greater resonance displacement for the same change in dielectric function (Figure 7d). The $\Delta\lambda_1$ and FWHM values for Au- and Ag-capped configurations are generally larger than those for Pd- and Mg-capped counterparts, which can be attributed to the *E*-field peaking at the metal/hydride interface and its weaker resonance compared to the metal/glass interface (Figure 7e). Additionally, the FoM for Au- and Ag-capped structures is typically higher than that of Pd- and Mg-capped ones at most ratios, reaching a maximum when the Pd thickness is 30 nm.

The situation changes fundamentally when Mg replaces Pd. The $\Delta\lambda_1$, FWHM, and FoM values for Mg-based structures are generally much larger than those for Pd-based counterparts, mainly due to the greater RI change in Mg after hydrogenation (Figure 7f). For Mg-on-top configurations (Mg/Au and Mg/Ag), the peak P1 red-shifts continuously as the Mg fraction grows, yet this advantage is nullified by dramatic broadening: FWHM inflates from about 40 nm to beyond 300 nm once Mg exceeds 60 nm, and FoM never surpasses 0.30. Hydriding turns metallic Mg ($\varepsilon' < 0$, $\varepsilon'' \approx 3$) into the low-loss dielectric MgH_2 ($\varepsilon' \approx +4$, $\varepsilon'' \approx 0$); the very interface that sustains the SPP therefore vanishes, converting the mode into radiative and ohmic loss and explaining the monotonic linewidth inflation and, eventually, the disappearance of a measurable resonance. The Au-based NAs show larger $\Delta\lambda_1$ that the Ag-based counterparts due to the larger *E*-field penetration of Au (Figure 7d). Placing the noble metal on top reverses the physics. In Ag/Mg and Au/Mg structures, the normal component of the *E*-field peaks at the metal/Mg interface, whereas in Mg-capped structures, it peaks at the metal/glass interface. The metal-to-dielectric transition within the buried layer induces a significant RI discontinuity, resulting in a much larger red-shift in the mode compared to Mg-capped counterparts (Figure 7e). A Mg thickness of merely 10 nm already produces a ~50 nm shift; at 40 nm Mg the shift reaches 163 nm for a Ag cap, while FWHM contracts to 80–130 nm. The resulting FoM attained is 1.96 for Ag (60 nm)/Mg (40 nm) and 1.10 for Au (70 nm)/Mg (30 nm), exceeding the best Pd-based values (<0.3) by an order of magnitude.

Contextualizing these findings underscores the advantages of the bilayer design in plasmonic hydrogen sensing. A single-layer Pd NA exhibits a resonance wavelength shift ($\Delta\lambda_1$) of 28 nm upon hydrogenation but suffers from a broad FWHM of ~200 nm, resulting in an FoM of ~0.14. Other nanostructures, whether single-layer or bilayer (composed of Pd, Mg, Ti, V, or Zr), lack a tracked P1 mode (as shown in Figures 1 and 2), resulting in poor sensor performance. Introducing a Au or Ag capping layer significantly enhances the FoM by more effectively narrowing the resonance linewidth, and also increases the wavelength shift through optimization of the material ratio and layer arrangement. The Ag (60 nm)/Mg (40 nm) bilayer is particularly noteworthy, achieving an FoM = 1.96 alongside large absolute resonance shifts ($\Delta\lambda$ = 163 nm) (Figure 7g), surpassing the best plasmonic hydrogen sensors reported to date [36,40,42,43,55–66], as summarized in Figure 7h. It should be noted that Ag is relatively stable in air, mainly being susceptible to tarnishing by sulfur compounds rather than rapid oxidation, and has been widely used in plasmonic sensors [67]. In the Ag/Mg bilayer, the Mg bottom layer is effectively protected from oxidation by the upper Ag film,

ensuring a degree of practical feasibility. Moreover, this cost-effective, earth-abundant architecture maintains the fabrication simplicity and broadband coupling characteristics of conventional EOT geometries based on colloidal lithography.

4. Conclusions

This work establishes stratified NAs as an effective platform for high-performance, intrinsically safe hydrogen sensing. Systematic FDTD calculations demonstrate that monometallic NA films present an unavoidable compromise: each monometallic NA satisfies only a subset of the desired sensing criteria. Pd provides readily traceable EOT resonances, yet the associated $\Delta\lambda$ and ΔT are comparatively small. Mg, in contrast, experiences the largest RI swing and therefore the largest spectral perturbation, but MgH_2 formation damps its surface plasmon modes and obscures spectral tracking. Ti, V, and Zr display both weak EOT signatures and modest spectral changes.

For the bilayer NAs composed of Pd, Mg, Ti, V, and Zr, incorporating Pd and/or Mg exhibit the most pronounced hydrogen responses, with the Mg/Pd configuration achieving much greater shifts in resonance wavelength and transmission than single-metal Pd or Mg. Pd-based bilayers retain key plasmonic features during hydrogen cycling, ensuring reliable sensing performance, whereas bilayers based on Ti, V, and Zr show minimal or even negative responses and significant spectral broadening, limiting their sensing utility. While the stacking order has a minor effect on specific modes, the choice of metal layers is the primary factor determining hydrogen sensitivity. However, hydride formation still leads to some damping of the resonances, indicating that further optimization—such as combining with strong plasmonic materials—is needed to maximize the figure of merit in bilayer plasmonic hydrogen sensors.

By vertically integrating a hydrogen-active layer (Pd or Mg) with a low-loss plasmonic cap (Au or Ag), we achieve independent control of chemical sensitivity and optical resonance, resulting in a maximized figure of merit (FoM). Au or Ag capping layers efficiently separate plasmon excitation from hydrogen transduction, allowing systematic tuning of resonance quality. Bilayer configurations with Pd or Mg sandwiched between Au (or Ag) and glass show enhanced resonance shifts and FoM, as the electric field is concentrated at the metal/hydride interface. Materials like Mg, which undergo a metal-to-dielectric transition upon hydrogenation, induce significantly larger refractive index changes and greater FoM enhancement than Pd. While Au caps yield larger wavelength shifts due to deeper field penetration, Ag provides narrower resonances. Increasing the thickness of the hydride-forming layer further amplifies both resonance shift and linewidth. The optimal Ag(60 nm)/Mg(40 nm) bilayer nanohole array yields a 163 nm resonance shift, 83 nm linewidth, and an FoM of 1.96—an order-of-magnitude improvement over state-of-the-art Pd devices.

Continuous-film geometry further suppresses nanoparticle fragmentation, ensuring mechanical integrity during repeated hydriding cycles, while compatibility with large-area colloidal lithography offers a low-cost, scalable route toward practical devices. Beyond the immediate performance gains, this theoretical study provides clear electromagnetic design rules: (i) generate high-quality surface plasmon polaritons with a noble-metal film; (ii) tune individual thicknesses to balance resonance sharpness against dielectric perturbation; and (iii) position a hydride-forming layer within the evanescent field to maximize modal overlap. These principles are general and can be transferred to other analyte–material combinations, paving the way for a broader class of remote, label-free optical sensors.

The proposed nanohole array design enables simplified optical setups with robust, low-cost components, while scalable fabrication methods such as colloidal lithography

support disposable or large-scale production. Enhanced packaging and signal processing further improve environmental stability. These developments, together with emerging portable and commercial SPR devices, indicate that our sensor design is well-suited for real-world applications in fields such as biomedical diagnostics, environmental monitoring, and industrial process control.

Supplementary Materials: The following supporting information can be downloaded at: https://www.mdpi.com/article/10.3390/chemosensors13080309/s1, Table S1: Quantitative comparison of representative hydrogen sensors; Table S2: $\Delta\lambda_1$, FWHM, and FoM of the single and bilayer nanohole arrays.

Author Contributions: B.A. conceptualized the research; J.F. and Y.L. performed the calculation and data analysis. X.C. and M.C. helped with the data analysis. B.A. wrote the paper with input from all authors. All authors have read and agreed to the published version of the manuscript.

Funding: This research was supported by National Natural Science Foundation of China (grant nos. 62105043).

Data Availability Statement: The datasets generated during the current study are available from the corresponding author upon written request.

Conflicts of Interest: The authors declare that they have no known competing financial interests or personal relationships that could have appeared to influence the work reported in this paper.

References

1. Evro, S.; Oni, B.A.; Tomomewo, O.S. Carbon neutrality and hydrogen energy systems. *Int. J. Hydrogen Energy* **2024**, *78*, 1449–1467. [CrossRef]
2. Kafil, V.; Sreenan, B.; Hadj-Nacer, M.; Wang, Y.; Yoon, J.; Greiner, M.; Chu, P.; Wang, X.; Fadali, M.S.; Zhu, X. Review of noble metal and metal-oxide-semiconductor based chemiresitive hydrogen sensors. *Sens. Actuators A Phys.* **2024**, *373*, 115440. [CrossRef]
3. Koo, W.-T.; Cho, H.-J.; Kim, D.-H.; Kim, Y.H.; Shin, H.; Penner, R.M.; Kim, I.-D. Chemiresistive hydrogen sensors: Fundamentals, recent advances, and challenges. *ACS Nano* **2020**, *14*, 14284–14322. [CrossRef] [PubMed]
4. Zhang, W.; Zou, J.; Sun, J.; Wang, W.; Shan, L.; Bao, K.; Gao, W.; Zhou, Y.; Jin, Q.; Jian, J. Fabrication and sensing performance of carrier-free catalytic combustion hydrogen sensors based on electrodeposition method. *Int. J. Hydrogen Energy* **2024**, *61*, 1356–1364. [CrossRef]
5. Henriquez, D.D.O.; Cho, I.; Yang, H.; Choi, J.; Kang, M.; Chang, K.S.; Jeong, C.B.; Han, S.W.; Park, I. Pt nanostructures fabricated by local hydrothermal synthesis for low-power catalytic-combustion hydrogen sensors. *ACS Appl. Nano Mater.* **2021**, *4*, 7–12. [CrossRef]
6. Korotcenkov, G.; Han, S.D.; Stetter, J.R. Review of electrochemical hydrogen sensors. *Chem. Rev.* **2009**, *109*, 1402–1433. [CrossRef] [PubMed]
7. Gorbova, E.; Balkourani, G.; Molochas, C.; Sidiropoulos, D.; Brouzgou, A.; Demin, A.; Tsiakaras, P. Brief review on high-temperature electrochemical hydrogen sensors. *Catalysts* **2022**, *12*, 1647. [CrossRef]
8. Gu, H.; Wang, Z.; Hu, Y. Hydrogen gas sensors based on semiconductor oxide nanostructures. *Sensors* **2012**, *12*, 5517–5550. [CrossRef]
9. Phanichphant, S. Semiconductor metal oxides as hydrogen gas sensors. *Procedia Eng.* **2014**, *87*, 795–802. [CrossRef]
10. Ivanov, I.I.; Baranov, A.M.; Talipov, V.A.; Mironov, S.M.; Akbari, S.; Kolesnik, I.V.; Orlova, E.D.; Napolskii, K.S. Investigation of catalytic hydrogen sensors with platinum group catalysts. *Sens. Actuators B Chem.* **2021**, *346*, 130515. [CrossRef]
11. Baranov, A.; Ivanov, I.; Karpova, E. Effects of Flameless Catalytic Combustion of Hydrogen on the Parameters of Catalytic Sensors with Platinum-group Catalysts. *Sens. Mater.* **2023**, *35*, 3585–3594. [CrossRef]
12. Gorbova, E.; Tzorbatzoglou, F.; Molochas, C.; Chloros, D.; Demin, A.; Tsiakaras, P. Fundamentals and principles of solid-state electrochemical sensors for high temperature gas detection. *Catalysts* **2021**, *12*, 1. [CrossRef]
13. Watanabe, M.; Inoue, R.; Ichikawa, D.; Furusaki, K. Development of thermal conductivity type hydrogen sensor. *ECS Trans.* **2010**, *28*, 31. [CrossRef]
14. Akasaka, S.; Terumoto, K.; Kanno, I. Temperature dependence of accuracy of thermal conductivity hydrogen sensor. In Proceedings of the 2024 IEEE SENSORS, Kobe, Japan, 20–23 October 2024; pp. 1–4.
15. Shubham, K.; Khan, R.; Chakrabarti, P. Investigation of Pd/TiO_2/Si MIS capacitor as hydrogen sensor. *Sens. Rev.* **2015**, *35*, 62–67. [CrossRef]

16. Kim, K.-S.; Chung, G.-S. Fast response hydrogen sensors based on palladium and platinum/porous 3C-SiC Schottky diodes. *Sens. Actuators B Chem.* **2011**, *160*, 1232–1236. [CrossRef]
17. Drake, C.; Deshpande, S.; Bera, D.; Seal, S. Metallic nanostructured materials based sensors. *Int. Mater. Rev.* **2007**, *52*, 289–317. [CrossRef]
18. Chaujar, R.; Yirak, M.G. Sensitivity investigation of junctionless gate-all-around silicon nanowire field-effect transistor-based hydrogen gas sensor. *Silicon* **2023**, *15*, 609–621. [CrossRef]
19. Tamersit, K. WS2 Nanosheet-Based Ultrascaled Field-Effect Transistor for Hydrogen Gas Sensing: Addressing the Sensitivity-Downscaling Trade-Off. *Sensors* **2024**, *24*, 6730. [CrossRef]
20. Cui, B.; Ren, Z.; Wang, W.; Cheng, L.; Gao, X.; Huang, L.; Hu, A.; Hu, F.; Jin, J. Review of surface acoustic wave-based hydrogen sensor. *Sens. Actuators Rep.* **2024**, *7*, 100197. [CrossRef]
21. Kim, S.; Singh, G.; Lee, K. Development of Highly Sensitive and Stable Surface Acoustic Wave-Based Hydrogen Sensor and Its Interface Electronics. *Adv. Mater. Technol.* **2022**, *7*, 2200180. [CrossRef]
22. Guruprasad, B.; Shwetha, M. Design and fabrication of cantilever MEMS sensor model for electro-chemical gas sensor. *Int. J. Eng. Res. Technol.* **2020**, *9*, 704–715. [CrossRef]
23. Poh, C.-K. Metallic Nanostructures, Ultrathin Films and Optical Technologies for Hydrogen Storage and Switchable Mirrors. Ph.D. Thesis, University of Wollongong, Wollongong, Australia, 2011.
24. Shen, C.; Xie, Z.; Huang, Z.; Yan, S.; Sui, W.; Zhou, J.; Wang, Z.; Han, W.; Zeng, X. Review of the status and prospects of fiber optic hydrogen sensing technology. *Chemosensors* **2023**, *11*, 473. [CrossRef]
25. Allsop, T.; Neal, R. A review: Application and implementation of optic fibre sensors for gas detection. *Sensors* **2021**, *21*, 6755. [CrossRef]
26. Pathak, A.K.; Verma, S.; Sakda, N.; Viphavakit, C.; Chitaree, R.; Rahman, B.A. Recent advances in optical hydrogen sensor including use of metal and metal alloys: A review. *Photonics* **2023**, *10*, 122. [CrossRef]
27. Chen, Z.; Wu, X.; Liu, H.; Baqir, M.A.; Yu, K.; Zhang, K. Hyperbolic metamaterials assisted ultrathin Pd films for high-sensitivity hydrogen sensors. *Int. J. Hydrogen Energy* **2024**, *81*, 812–818. [CrossRef]
28. Ai, B.; Sun, Y.; Zhao, Y. Plasmonic Hydrogen Sensors. *Small* **2022**, *18*, e2107882. [CrossRef]
29. Darmadi, I.; Östergren, I.; Lerch, S.; Lund, A.; Moth-Poulsen, K.; Müller, C.; Langhammer, C. Bulk-Processed Plasmonic Plastic Nanocomposite Materials for Optical Hydrogen Detection. *Acc. Chem. Res.* **2023**, *56*, 1850–1861. [CrossRef]
30. Li, C.; Zheng, F.; Mi, X.; Wei, B.; Zhang, X. Pd-based eye-readable H2 sensors: Principles, developments, and perspectives. *Opt. Laser Technol.* **2024**, *176*, 110955. [CrossRef]
31. Mayer, K.M.; Hafner, J.H. Localized surface plasmon resonance sensors. *Chem. Rev.* **2011**, *111*, 3828–3857. [CrossRef]
32. Sil, D.; Gilroy, K.D.; Niaux, A.; Boulesbaa, A.; Neretina, S.; Borguet, E. Seeing Is Believing: Hot Electron Based Gold Nanoplasmonic Optical Hydrogen Sensor. *ACS Nano* **2014**, *8*, 7755–7762. [CrossRef] [PubMed]
33. Matuschek, M.; Singh, D.P.; Jeong, H.H.; Nesterov, M.; Weiss, T.; Fischer, P.; Neubrech, F.; Liu, N. Chiral Plasmonic Hydrogen Sensors. *Small* **2018**, *14*, 1702990. [CrossRef]
34. Adams, B.D.; Chen, A. The role of palladium in a hydrogen economy. *Mater. Today* **2011**, *14*, 282–289. [CrossRef]
35. Wang, T.; Tang, L.; Zhang, Y.; Hong, Z.; Liu, G.; Li, Z.; Chen, J.; Peng, L.; Ding, W. Interaction between Hydrogen and Magnesium Films: From Hydrogenochromism to Applications. *ACS Appl. Mater. Interfaces* **2025**, *17*, 8794–8820. [CrossRef]
36. Palm, K.J.; Murray, J.B.; Narayan, T.C.; Munday, J.N. Dynamic Optical Properties of Metal Hydrides. *ACS Photonics* **2018**, *5*, 4677–4686. [CrossRef]
37. Strohfeldt, N.; Tittl, A.; Schaferling, M.; Neubrech, F.; Kreibig, U.; Griessen, R.; Giessen, H. Yttrium Hydride Nanoantennas for Active Plasmonics. *Nano Lett.* **2014**, *14*, 1140–1147. [CrossRef]
38. Liu, N.; Tang, M.L.; Hentschel, M.; Giessen, H.; Alivisatos, A.P. Nanoantenna-enhanced gas sensing in a single tailored nanofocus. *Nat. Mater.* **2011**, *10*, 631–636. [CrossRef] [PubMed]
39. Wy, Y.; Lee, S.; Wi, D.H.; Han, S.W. Colloidal clusters of bimetallic core–shell nanoparticles for enhanced sensing of hydrogen in aqueous solution. *Part. Part. Syst. Charact.* **2018**, *35*, 1700380. [CrossRef]
40. Nugroho, F.A.A.; Darmadi, I.; Cusinato, L.; Susarrey-Arce, A.; Schreuders, H.; Bannenberg, L.J.; Fanta, A.B.D.; Kadkhodazadeh, S.; Wagner, J.B.; Antosiewicz, T.J.; et al. Metal-Polymer Hybrid Nanomaterials for Plasmonic Ultrafast Hydrogen Detection. *Nat. Mater.* **2019**, *18*, 489–495. [CrossRef] [PubMed]
41. Ai, B.; Yu, Y.; Möhwald, H.; Zhang, G.; Yang, B. Plasmonic films based on colloidal lithography. *Adv. Colloid Interface Sci.* **2014**, *206*, 5–16. [CrossRef]
42. Luong, H.M.; Pham, M.T.; Madhogaria, R.P.; Phan, M.-H.; Larsen, G.K.; Nguyen, T.D. Bilayer Plasmonic Nano-Lattices for Tunable Hydrogen Sensing Platform. *Nano Energy* **2020**, *71*, 104558. [CrossRef]
43. Shen, Y.; She, X.Y.; Jin, C.J. Mechanically Reconfigurable Pd Nanogroove Array: An Ultrasensitive Optical Hydrogen Detector. *ACS Photonics* **2018**, *5*, 1334–1342. [CrossRef]

44. Ebbesen, T.W.; Lezec, H.J.; Ghaemi, H.; Thio, T.; Wolff, P.A. Extraordinary optical transmission through sub-wavelength hole arrays. *Nature* **1998**, *391*, 667–669. [CrossRef]
45. Garcia-Vidal, F.J.; Martin-Moreno, L.; Ebbesen, T.; Kuipers, L. Light passing through subwavelength apertures. *Rev. Mod. Phys.* **2010**, *82*, 729–787. [CrossRef]
46. Zhang, X.; Li, Z.; Ye, S.; Wu, S.; Zhang, J.; Cui, L.; Li, A.; Wang, T.; Li, S.; Yang, B. Elevated Ag nanohole arrays for high performance plasmonic sensors based on extraordinary optical transmission. *J. Mater. Chem.* **2012**, *22*, 8903–8910. [CrossRef]
47. Lee, S.H.; Bantz, K.C.; Lindquist, N.C.; Oh, S.-H.; Haynes, C.L. Self-assembled plasmonic nanohole arrays. *Langmuir* **2009**, *25*, 13685–13693. [CrossRef]
48. Chang, S.-H.; Gray, S.K.; Schatz, G.C. Surface plasmon generation and light transmission by isolated nanoholes and arrays of nanoholes in thin metal films. *Opt. Express* **2005**, *13*, 3150–3165. [CrossRef]
49. Maystre, D. Theory of Wood's anomalies. In *Plasmonics: From Basics to Advanced Topics*; Springer: Berlin/Heidelberg, Germany, 2012; pp. 39–83.
50. Duan, X.; Liu, N. Magnesium for Dynamic Nanoplasmonics. *Acc. Chem. Res.* **2019**, *52*, 1979–1989. [CrossRef]
51. Zhang, H.; Zheng, J.; Xia, X.; Shao, L.; Wang, J. Chapter 2—Plasmonic nanomaterials: Noble metals and beyond. In *Plasmonic Materials and Metastructures*; Gwo, S., Alù, A., Li, X., Shih, C.-K., Eds.; Elsevier: Amsterdam, The Netherlands, 2024; pp. 35–72.
52. Vollmer, F.; Arnold, S. Whispering-gallery-mode biosensing: Label-free detection down to single molecules. *Nat. Methods* **2008**, *5*, 591–596. [CrossRef]
53. Bogaerts, W.; De Heyn, P.; Van Vaerenbergh, T.; De Vos, K.; Kumar Selvaraja, S.; Claes, T.; Dumon, P.; Bienstman, P.; Van Thourhout, D.; Baets, R. Silicon microring resonators. *Laser Photonics Rev.* **2012**, *6*, 47–73. [CrossRef]
54. Maier, S.A. *Plasmonics: Fundamentals and Applications*; Springer: New York, NY, USA, 2007; Volume 1.
55. Lv, X.; Wu, F.; Tian, Y.; Zuo, P.; Li, F.; Xu, G.; Niu, W. Engineering the Intrinsic Chirality of Plasmonic Au@Pd Metamaterials for Highly Sensitive Chiroplasmonic Hydrogen Sensing. *Adv. Mater.* **2023**, *35*, 2305429. [CrossRef]
56. Nugroho, F.A.A.; Bai, P.; Darmadi, I.; Castellanos, G.W.; Fritzsche, J.; Langhammer, C.; Gómez Rivas, J.; Baldi, A. Inverse designed plasmonic metasurface with parts per billion optical hydrogen detection. *Nat. Commun.* **2022**, *13*, 5737. [CrossRef] [PubMed]
57. Liao, C.R.; Xiong, C.; Zhao, J.L.; Zou, M.Q.; Zhao, Y.Y.; Li, B.Z.; Ji, P.; Cai, Z.H.; Gan, Z.S.; Wang, Y.; et al. Design and realization of 3D printed fiber-tip microcantilever probes applied to hydrogen sensing. *Light—Adv. Manuf.* **2022**, *3*, 3–13. [CrossRef]
58. Xu, F.; Ma, J.; Hu, K.; Zhang, Z.; Ma, C.; Guan, B.-O.; Chen, K. Ultrahigh sensitivity of hydrogen detection with a perforated Pd film on a miniature fiber tip. *Sens. Actuators B Chem.* **2024**, *400*, 134875. [CrossRef]
59. Lin, X.; Cheng, M.; Chen, X.; Zhang, J.; Zhao, Y.; Ai, B. Unlocking Predictive Capability and Enhancing Sensing Performances of Plasmonic Hydrogen Sensors via Phase Space Reconstruction and Convolutional Neural Networks. *ACS Sens.* **2024**, *9*, 3877–3888. [CrossRef]
60. Cheng, M.; Lin, X.; Chen, X.; Chen, C.; Zhang, G.; Ai, B. Enhancing Plasmonic Hydrogen Sensing Through Heterogeneous Multilayer Configurations with Quantitative Mechanism Analysis. *ACS Appl. Nano Mater.* **2024**, *7*, 14203–14212. [CrossRef]
61. Subramanian, S.; Kumar, K.; Dhawan, A. Palladium-coated narrow groove plasmonic nanogratings for highly sensitive hydrogen sensing. *RSC Adv.* **2020**, *10*, 4137–4147. [CrossRef]
62. Farnood, A.; Ranjbar, M.; Salamati, H. Localized Surface Plasmon Resonance (LSPR) Detection of Hydrogen Gas by Pd^{2+}/Au Core/Shell Like Colloidal Nanoparticles. *Int. J. Hydrogen Energy* **2020**, *45*, 1158–1169. [CrossRef]
63. Darmadi, I.; Nugroho, F.A.A.; Kadkhodazadeh, S.; Wagner, J.B.; Langhammer, C. Rationally Designed PdAuCu Ternary Alloy Nanoparticles for Intrinsically Deactivation-Resistant Ultrafast Plasmonic Hydrogen Sensing. *ACS Sens.* **2019**, *4*, 1424–1432. [CrossRef]
64. Beni, T.; Yamasaku, N.; Kurotsu, T.; To, N.; Okazaki, S.; Arakawa, T.; Balcytics, A.; Seniutinas, G.; Juodkazis, S.; Nishijima, Y. Metamaterial for Hydrogen Sensing. *ACS Sens.* **2019**, *4*, 2389–2394. [CrossRef]
65. Wang, M.M.; Wang, P.; Zhang, J.; Hou, H.; Li, C.P.; Jin, Y.D. Pd/Ag nanosheet as a plasmonic sensing platform for sensitive assessment of hydrogen evolution reaction in colloid solutions. *Nano Res.* **2018**, *11*, 2093–2103. [CrossRef]
66. Houlihan, N.M.; Karker, N.; Potyrailo, R.A.; Carpenter, M.A. High Sensitivity Plasmonic Sensing of Hydrogen over a Broad Dynamic Range Using Catalytic Au-CeO_2 Thin Film Nanocomposites. *ACS Sens.* **2018**, *3*, 2684–2692. [CrossRef] [PubMed]
67. Gahlaut, S.K.; Pathak, A.; Gupta, B.D. Recent Advances in Silver Nanostructured Substrates for Plasmonic Sensors. *Biosensors* **2022**, *12*, 713. [CrossRef] [PubMed]

Disclaimer/Publisher's Note: The statements, opinions and data contained in all publications are solely those of the individual author(s) and contributor(s) and not of MDPI and/or the editor(s). MDPI and/or the editor(s) disclaim responsibility for any injury to people or property resulting from any ideas, methods, instructions or products referred to in the content.